

9th CIRP Conference on Assembly Technology and Systems

Gripper integrated vision guided assembly of PEM fuel cells

Jens Schäfer*, Simeon Allmendinger, Jürgen Fleischer

wbk Institute of Production Science, Karlsruhe Institute of Technology, Kaiserstraße 12, 76131 Karlsruhe, Germany

* Corresponding author. Tel.: +49 1523 9502613; E-mail address: jens.schaefer@kit.edu

Abstract

Polymer electrolyte membrane (PEM) fuel cells consist of hundreds of individual layers, which need to be precisely stacked onto each other in a pick-and-place process in order to ensure a functioning product. Common automated pick-and-place systems usually feature an external camera for position detection of the individual layers. However, an external position detection increases cycle time and reduces the overall efficiency of the assembly system. Thus, this approach presents a camera, which is integrated into a flat surface vacuum gripper to detect and measure the position of components on-the-fly while grasping. The camera makes use of the suction openings necessary for grasping itself. Incoming light is detected and an aperture photometry is being applied to the image. Different methods for the component position detection will be presented and compared to a precise stereo camera reference measurement for the components actual position. With the reference the measurement accuracy of the novel gripper configuration is derived.

© 2022 The Authors. Published by Elsevier Ltd.

This is an open access article under the CC BY-NC-ND license (<https://creativecommons.org/licenses/by-nc-nd/4.0>)

Peer-review under responsibility of the scientific committee of the 9 th CIRP Conference on Assembly Technology and Systems

Keywords: Fuel cell; Positioning; Assembly

1. Introduction

Polymer electrolyte membrane (PEM) fuel cell vehicles offer a high range with short refueling times compared to other zero emission vehicles, which especially gains relevance for long haul transportation. To generate enough power a so-called fuel cell stack consists of up to 400 individual cells stacked onto each other and thereby connected among themselves in series [1]. Due to the high number of components fast processes with short cycle time are required.

2. State of the art

A fuel cell stack is made of bipolar plates and membrane electrode assemblies (MEA), which create the repeating unit of a fuel cell. The bipolar plate is made out of thin metal or graphite and is responsible for gas distribution on the anode and cathode side as well as for internal cooling [2]. The MEA is made of a polymer electrolyte membrane (PEM) coated with catalyst (CCM, catalyst coated membrane). Designs vary [3], usually the CCM is framed in a subgasket with an anode and cathode gas diffusion layer (GDL) on opposite sides. These two components, bipolar plate and MEA, are the starting product for the fuel cell stack. In this particular stacking process both MEA and bipolar plate need to be stacked alternately. To avoid leakage and allow for a uniform pressure distribution it is mandatory to stack precisely [4]. Yet, with the MEA being made of thin foils, a mechanical alignment is not well suited

Nomenclature

X_{AB}, Y_{AB}	distance between points A and B
φ	component rotation
X_{CAM}, Y_{CAM}	calculated position of the component
X_{GOM}, Y_{GOM}	measured position of the component

for the MEA and can cause jamming for the bipolar plate [5]. Therefore, the alignment in automated machines needs to be carried out by optical systems. Common process sequences include individual grasping of the components, a camera measurement and a corrected placement. In [6,7] an approach is presented to avoid separate process times included in an alignment process. The camera is mounted overhead at the pick station as well as at the placement station. With an AI approach the accuracy of the system is increased. However, it is mentioned, that the component's structure limits further optimization. Both components, bipolar plate and MEA, do not lie flat. Shape deviation of the bipolar plate is caused by bending [8] and welding processes [9] whilst manufacturing. The MEA with its thin foils can also have shape errors due to residual stress whilst manufacturing or humidity change [10]. These characteristics cause the components to deform slightly whilst gripping and releasing that cause positioning errors. With the position measured whilst gripping these errors can be reduced. In [11] a method is described, that allows for an optimized utilization of the gripper inherent suction openings for position detection. However, the results are conceptual and have not been applied to an actual gripper.

3. Concept of a camera integrated gripper

In this paper we want to integrate an optical position measurement system into the gripper. Therefore a flat surface gripper will be utilized to gather information of the individual component's position, with the choice of materials being limited due to electrostatic behavior and anti-stick coating of the surface. For this purpose, a hole pattern has been generated to support the position detection with a camera located in the inside of the gripper, as described in [11].

A flat surface gripper is manufactured and equipped with a vacuum generator. The gripper plate itself is manufactured by a 3D-printer as various patterns can easily be generated, however, in later iterations the manufacturing method might change to a better suited process to increase the accuracy of the hole pattern. The camera is mounted inside the gripper, with a transparent surface between the camera and the gripper surface to allow for a vacuum generation, as shown in Fig. 1.

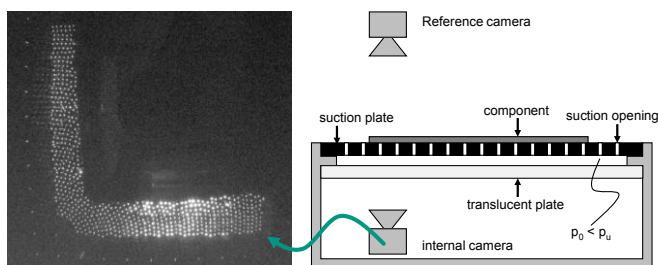


Fig. 1. Experimental setup for image acquisition (right) and obtained images (left)

The internal camera has a resolution of 670 by 619 pixels in the investigated camera frame that measures 110 mm by 100 mm, which equals to about 6 pixels per 1 mm. To generate reference measurements an additional measurement system (GOM ATOS Core) is included. Circular reference points are placed onto the component as well as onto the gripper. With

GOM's measurement suite a component inherent coordinate system can be derived from these points. In addition, the same method is applied on the gripper itself. Within the measurement suite the relative position and orientation of these two coordinate systems can be calculated.

On this setup the components position is randomly changed. For each new position an image is made with both, the internal camera and the external GOM measurement system. For our analysis a total of 100 images were made.

3.1. Image pre-processing and hole identification

Before further image processing, the camera is calibrated with a chessboard. In order to make a position measurement the individual holes of uncovered parts of the gripper need to be acquired. There are several options for hole recognition mostly based on Canny-edge algorithms and Hough transformation [12]. However, these algorithms mainly make use of gradients in brightness and therefore require a certain minimal size and light intensity. In contrast aperture photometry has been used in astronomy very early and allows for a highly precise determination of star center points in the sky, even with a width of solely a couple of pixels [13]. Since the required image evaluation must fulfill similar functions this concept is adopted.

3.2. Points matching

In addition, to be able to further calculate the exact positions the uncovered hole pattern is compared to the CAD files with regard to their respective x- and y- coordinates. The comparison between camera image and the CAD-file is implemented with a perspective-3-point algorithm as described in [14]. This way it is possible to correlate single pixel points with their respective coordinates obtained from CAD data.

4. Image analysis

The relationship between the camera coordinate system and the gripper coordinate system is shown in Fig. 2. With the given method of reference measurement on the rather thin foil the components edge on the outside cannot be used as reference.

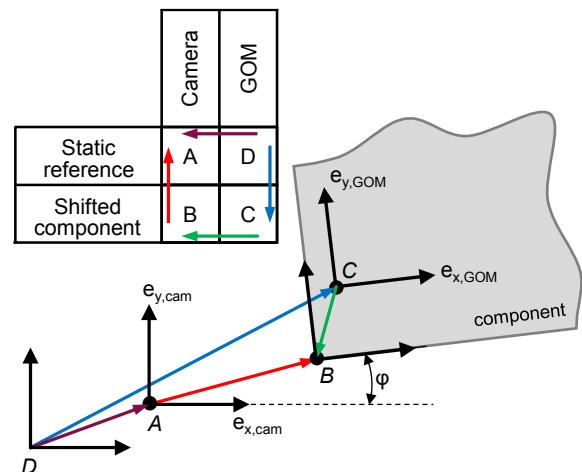


Fig. 2. Coordinate systems

Both, GOM (D) and the camera (A), feature a static origin, which is not located on the same spot. However, the distance between those stays the same and there is no rotation between the two. Additionally, both GOM and the camera are able to measure the components position on different characteristic traits: The camera measures the corner position (B) whereas GOM makes use of individual markers (C). Based on the components coordinates (e_{GOM}) their distance (x_{CB} , y_{CB}) stays the same, but when calculated in the camera coordinate system (e_{cam}) the angle of rotation (φ) has to be taken into consideration, as seen in equation (1).

$$\begin{aligned} CB &= C + x_{CB}e_{x,GOM} + y_{CB}e_{y,GOM} \\ &= C + (x_{CB}\sin(\varphi) + y_{CB}\cos(\varphi))e_{x,cam} \\ &\quad + (x_{CB}\cos(\varphi) - y_{CB}\sin(\varphi))e_{y,cam} \end{aligned} \quad (1)$$

Although being constant throughout all the images the distance from C to B is unknown and therefore needs to be calculated based on the experimental data. With DC being the same distance as $DA + AB - CB$ the following equations can be set up:

$$\vec{DC} = \vec{AD} - \vec{CB} \quad (2)$$

$$\begin{aligned} x_{GOM} &= x_{AD} + x_{cam} + x_{CB}\sin(\varphi) + y_{CB}\cos(\varphi) \\ y_{GOM} &= y_{AD} + y_{cam} + x_{CB}\cos(\varphi) - y_{CB}\sin(\varphi) \end{aligned} \quad (3)$$

$$\begin{aligned} x_{GOM} - x_{cam} &= (x_{AD}, y_{AD}, x_{CB}, y_{CB}) \\ &\quad * (1, 0, \sin(\varphi), \cos(\varphi))^T \\ y_{GOM} - y_{cam} &= (x_{AD}, y_{AD}, x_{CB}, y_{CB}) \\ &\quad * (0, 1, \cos(\varphi), -\sin(\varphi))^T \end{aligned} \quad (4)$$

With equation (4) a least-square approximation can then be performed to obtain the unknown values x_{AD} , y_{AD} , x_{CB} and y_{CB} based on both, the GOM Measurement (x_{GOM} , y_{GOM}) and the camera measurement (x_{CAM} , y_{CAM}).

4.1. Method one: best-fit through the edge points

The image is split into two regions of interest. With one the horizontal line is calculated, with the other one the vertical line is calculated. The calculation itself includes ten rightmost points for the vertical line and ten upmost points for the horizontal line. The intersection of those two lines then is considered as the x- and y-position of the component (x_{CAM} , y_{CAM}). This method is limited to rectangular objects or at least shapes with piecewise straight lines in it. Only the visible points are included, thus, the shape of the component always exceeds the actual size. This is due to the fact that the true edge of the layer is located directly next to the visible points. In Fig. 3 the approach is shown for a horizontal line with the visible points marked black and the four upmost points circled in red and the assumed edge position as a dashed line. In general, this approach is only suitable for small angles of rotation, since the regions of interest have fixed positions.

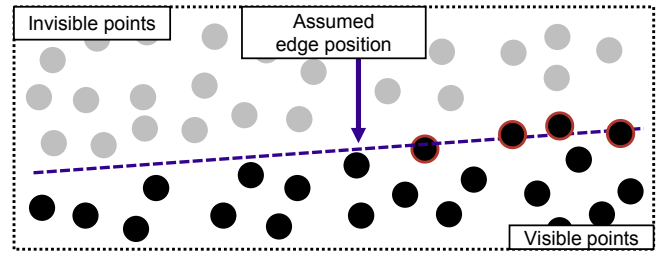


Fig. 3. Schematic illustration for the assumed edge position (method one)

4.2. Method two: best-fit through visible and invisible edge points with perpendicularity condition

In this approach, the invisible points are included in the calculation. Since the x- and y-position of all suction holes is predefined, covered ones can easily be located with the perspective-3-point algorithm. On this basis, the edge detection can be improved due to the true position of the layer's edge between invisible and visible suction holes (points). Similar to the previous method, ten visible points are used each for the calculation of the vertical and horizontal lines. This now also offers the chance to predict layer edges between visible and invisible points.

All visible points are separated into ten intervals beforehand, ensuring the correct detection even for strongly rotated layers (Fig. 4). In addition, one invisible point for each interval further decreases the error of detection. Thus, twenty points are regressed describing the assumed edge position. Moreover, both the horizontal and vertical line are defined as perpendicular. Consequently, the total regression error is minimized simultaneously. The intersection of the vertical and horizontal line determines the x- and y-position of the component (x_{CAM} , y_{CAM}).

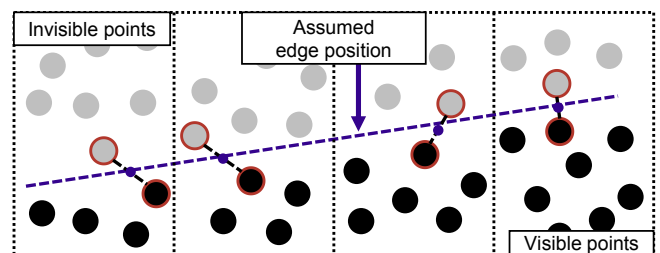


Fig. 4. Schematic illustration for the assumed edge position acquisition (method two)

4.3. Method three: best-fit through the edge points with perpendicularity condition and brightness consideration

Regarding method two, brightness considerations are not included in the calculation of the edge detection. Yet, especially partly covered holes at the considered corner give highly accurate information about the components edge position as seen in Fig. 5 with completely illuminated points marked yellow and partly illuminated points marked red. For this reason, method two was expanded by a weighting factor in accordance with the flux of a single hole. Thus, those points are

rewarded which have a reduced brightness and are only partially shielded by the layer, since these are very likely to be below the edge of the layer.

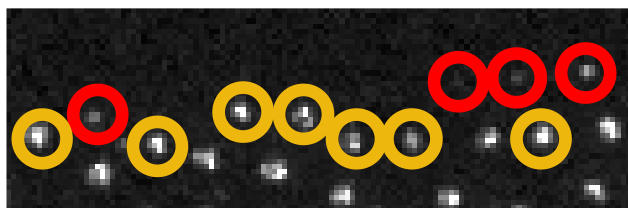


Fig. 5. Camera image with full illuminated holes (yellow) and partly illuminated holes (red)

5. Results

The three methods presented are implemented with the displacement between the coordinate systems A and D being calculated (x_{AD}, y_{AD}) as well as the distance between A and B (x_{GOM}, y_{GOM}) via a least-square approach based on equation (4). With the results the difference of the right-hand side and left-hand side of equation (3) is calculated and the standard deviation for the corresponding x- and y-values are derived. The results including coefficients of determination are shown in Table 1.

Table 1. Comparison of results for the different methods

	Method one	Method two	Method three
x_{AD}	- 91.30 mm	-93.02 mm	-93.47 mm
y_{AD}	- 75.67 mm	-85.22 mm	-84.94 mm
x	4.92 mm	7.24 mm	7.64 mm
y	0.09 mm	9.57 mm	9.29 mm
r^2	48.09 mm ²	11.13 mm ²	9.93 mm ²
deviation (x)	0.343 mm	0.247 mm	0.244 mm
deviation (y)	0.603 mm	0.225 mm	0.199 mm

With method two more accurate results can be obtained compared to method one if comparing the standard deviation. In comparing the offset values it becomes clear, that there is systematic offset, as the position is always calculated too close to the visible points. With the herein presented approach the offset cannot be directly calculated, however x_{GOM} and y_{GOM} values suggest so. For method three the standard deviation of the errors is slightly smaller compared to method two, mainly due to some outliers as shown in Fig. 6.

The faulty results and outliers in method three are caused by non-homogenous illumination, therefore undermining the strategy. Possible development could utilize the brightness of neighboring suction openings, as it is very unlikely that there is a high variation in openings next to each other. When comparing it to the camera resolution of about 6 pixels per 1 mm the results show that there is nearly no lack of accuracy despite the non-transparent suction plate in between.

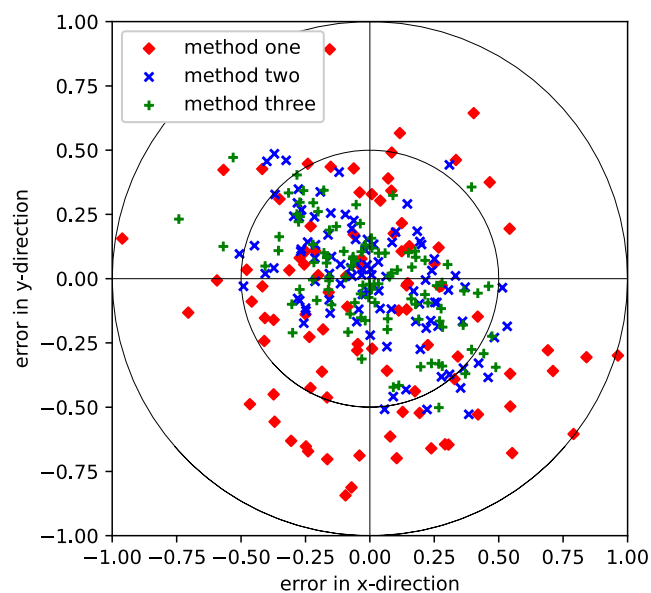


Fig. 6. Comparison of errors in x- and y-direction for the presented methods

6. Conclusion

With the gripper presented it was possible to determine the components position relative to the gripper while grasping. As the measurement takes place during gripping and does not require for a separate measurement station the cycle times in pick-and-place processes can be reduced. However, for the application in fuel cell stacking the accuracy needs to be improved. With these experimental findings the generation for the patterns can be enhanced further, allowing for a higher precision.

7. Acknowledgements

The authors would like to thank the Federal Ministry of Transportation and Digital Infrastructure for funding the project EMSigBZ (Grant No. 03B11012C) in the National Innovation Program Hydrogen and Fuel Cell Technology (NIP).

8. References

- [1] Yoshida T, Kojima K. Toyota MIRAI Fuel Cell Vehicle and Progress Toward a Future Hydrogen Society. *Interface magazine* 2015;24(2):45–9. <https://doi.org/10.1149/2.F03152if>.
- [2] Herrmann A, Chaudhuri T, Spagnol P. Bipolar plates for PEM fuel cells: A review. *International Journal of Hydrogen Energy* 2005;30(12):1297–302. <https://doi.org/10.1016/j.ijhydene.2005.04.016>.
- [3] Stahl P. Edge effects on the single cell level of polymer electrolyte fuel cells: Universität Stuttgart.
- [4] Liang P, Qiu D, Peng L, Yi P, Lai X, Ni J. Contact resistance prediction of proton exchange membrane fuel cell considering fabrication characteristics of metallic bipolar plates. *Energy Conversion and Management* 2018;169:334–44. <https://doi.org/10.1016/j.enconman.2018.05.069>.

- [5] Song K, Wang Y, Ding Y, Xu H, Mueller-Welt P, Stuermlinger T et al. Assembly techniques for proton exchange membrane fuel cell stack: A literature review. *Renewable and Sustainable Energy Reviews* 2022;153(1):111777. <https://doi.org/10.1016/j.rser.2021.111777>.
- [6] Bobka P, Gabriel F, Dröder K. Fast and precise pick and place stacking of limp fuel cell components supported by artificial neural networks. *CIRP Annals* 2020;69(1):1–4. <https://doi.org/10.1016/j.cirp.2020.04.103>.
- [7] Bobka P, Gabriel F, Römer M, Engbers T, Willgeroth M, Dröder K. Fast Pick and Place Stacking System for Thin, Limp and Inhomogeneous Fuel Cell Components. In: Wulfsberg JP, Hintze W, Behrens B-A, editors. *Production at the leading edge of technology*. Berlin, Heidelberg: Springer Berlin Heidelberg; 2019, p. 389–399.
- [8] Xu S, Li K, Wei Y, Jiang W. Numerical investigation of formed residual stresses and the thickness of stainless steel bipolar plate in PEMFC. *International Journal of Hydrogen Energy* 2016;41(16):6855–63. <https://doi.org/10.1016/j.ijhydene.2016.03.005>.
- [9] Yi P, Du X, Kan Y, Peng L, Lai X. Modeling and experimental study of laser welding distortion of thin metallic bipolar plates for PEM fuel cells. *International Journal of Hydrogen Energy* 2015;40(14):4850–60. <https://doi.org/10.1016/j.ijhydene.2015.02.025>.
- [10] Uchiyama T, Kato M, Yoshida T. Buckling deformation of polymer electrolyte membrane and membrane electrode assembly under humidity cycles. *Journal of Power Sources* 2012;206:37–46. <https://doi.org/10.1016/j.jpowsour.2012.01.073>.
- [11] Schäfer J, Allmendinger S, Hofmann J, Fleischer J. Genetic algorithm for the optimization of vision acquisition for on-the-fly position measurement of individual layers in fuel cell stack assembly. *Procedia CIRP* 2021;104:1407–11. <https://doi.org/10.1016/j.procir.2021.11.237>.
- [12] Yuen HK, Princen J, Illingworth J, Kittler J. Comparative study of Hough Transform methods for circle finding. *Image and Vision Computing* 1990;8(1):71–7. [https://doi.org/10.1016/0262-8856\(90\)90059-E](https://doi.org/10.1016/0262-8856(90)90059-E).
- [13] Mighell KJ. Algorithms for CCD Stellar Photometry. In: Mehringer DM, editor. *Astronomical data analysis software and systems VIII: Proceedings of a meeting held at Urbana, Illinois, USA, 1 - 4 November, 1998*. San Francisco, Calif.: Astronomical Soc. of the Pacific; 1999, p. 317–328.
- [14] Gao X-S, Hou X-R, Tang J, Cheng H-F. Complete solution classification for the perspective-three-point problem. *IEEE Trans. Pattern Anal. Machine Intell.* 2003;25(8):930–43. <https://doi.org/10.1109/TPAMI.2003.1217599>.